Pharmacophore and QSAR Modeling of Endothelial Nitric Oxide Synthase Inhibitors and Subsequent Validation and *In Silico* Search for New Hits

Ghadeer A. R. Y. Suaifan[1], Heba A. N. Al-Ejal[1], Mutasem O. Taha[1]*

[1] Department of Pharmaceutical Sciences, Faculty of Pharmacy, University of Jordan, Amman, Jordan, Telephone: 00962 6 5355000 ext. 23305, Fax: 00962 6 5339649

ABSTRACT

Endothelial Nitric Oxide synthase (eNOS) has an emerging role in chronic inflammation and cancer thus prompting continuous attempts to discover new inhibitors of this enzyme. Towards this end, efforts to discover and optimize new eNOS inhibitors are essential. Therefore, we explored the pharmacophoric space of 151 eNOS inhibitors using ten diverse sets of inhibitors to identify high quality pharmacophores. Subsequently, genetic algorithm and multiple linear regression analysis were employed to select an optimal combination of pharmacophoric models and 2D physicochemical descriptors capable of accessing a self-consistent quantitative structure-activity relationship (QSAR) of optimal predictive potential ($r^2_{121} = 0.77$, F = 63.5, $r^2_{LOO} = 0.62$, and r^2_{PRESS} against 30 external test inhibitors = 0.63). Interestingly, only one pharmacophore emerged in the optimal QSAR equation. Comparisons with the binding site of eNOS and receiver-operating characteristic (ROC) curves analysis established the validity of this QSAR-selected pharmacophore model. We employed the pharmacophoric model and associated QSAR equation to screen the national cancer institute list of compounds (NCI).

Keywords: Endothelial Nitric Oxide Synthase, Quantitative Structure Activity Relationship, *In silico* screening, Pharmacophore modeling.

INTRODUCTION

Nitric oxide $(NO)^{1-2}$, is a double-edged sword molecule, beneficial as a messenger or modulator for immunological self-defense but at the same time, potentially toxic upon excessive production.[1] Nitric oxide is synthesized by a family of enzymes called nitric oxide synthases (NOS),[2] which catalyze the oxidation of L-arginine to L-citrulline and nitric oxide. Classically, three distinct isoforms of NOS have been identified and characterized as products of different genes, with different subcellular localization, regulation, catalytic properties, and inhibitor sensitivity: endothelial NOS

(eNOS) and neuronal NOS (nNOS), expressed constitutively in the vascular endothelium and in the nervous system, respectively. nNOS acts as a neurotransmitter[3] while eNOS regulates the blood pressure and the vascular tone.[4-6] The third isoform is inducible NOS (iNOS) which generates high levels of NO that plays an important role in the regulation of immune reactions.[7, 8]

Obviously, under- and over-production of NO is responsible for a number of pathological conditions. Underproduction of NO by eNOS causes hypertension and atherosclerosis.[9] Whereas overproduction has recently been reported to modulate cancer-related events (angiogenesis, apoptosis, cell cycle, invasion, and metastasis).[10] In fact, clinical studies on human colon cancer samples suggest that a high eNOS expression can

*Corresponding Author: Email: mutasem@ju.edu.jo

be positively correlated with tumor cell vascular invasion[11] and trophoblast cancer cell vascular invasion.[12] On the other hand, overproduction of NO by brain nNOS is associated with stroke and chronic neurodegenerative diseases, such as Alzheimer's, Parkinson's, and Huntington's diseases.[13] Whereas overproduction of iNOS is implicated in tissue damage and cell apoptosis following inflammation and ischemia, rheumatoid arthritis, onset of Colitis[14] and cancer[15]. Appreciation of the pathological roles of eNOS-derived NO has stimulated interest in the discovery of novel eNOS inhibitors for potential therapeutic use in cancer prevention and treatment.

There is a bewildering array of NOS inhibitors described in the literature. The prototypical NOS inhibitors were analogs of L-arginine such as N^G-nitro-L-arginine (L-NNA)[16] and N^G-monomethyl-L-arginine (L-NMMA)[17]. Non-L-arginine type NOS inhibitors such as N^δ-iminomethyl-L-ornithine[18], *S*-alkyl-L-thiocitrulline[19], and (1*S*,4*S*,6*R*,7*R*) 7-chloro-3-imino-5-methyl-2-azabicyclo(4.1.0) heptane-hydrochloride (ONO-1714)[20] were also investigated and reported to exhibit potent inhibition with variable selectivity for NOS and its isoforms. These inhibitors have been investigated as mechanism-based inactivators of nitric oxide synthase. Their inhibitory effects are caused by competition with the natural substrate of NOS, L-arginine, in the binding site and/or in the oxidizing center of the enzyme (heme) or by the interaction with peptide motifs of the enzyme that influence its dimerization, affinity for cofactors, and interaction with associated proteins.[21-23]

In the last few years extensive structure-based investigations were carried out on NOS inhibitors to understand their mechanisms of inhibition, interactions within the enzymatic catalytic site, time dependence and selectivity for individual isoforms. Several crystal structures have been solved for truncated oxygenase domains of bovine eNOS and human eNOS[24] with a variety of bound ligands. Recently, Aparna et al[25] have reported a molecular dynamics study on NOS isoforms. Several other workers also employed the structure-based design methods to obtain new NOS lead ligands.[26-30]

However, the main focus of recent efforts towards the development of new eNOS inhibitors has concentrated on the structure-based ligand design[31-33], e.g., de novo design/docking[34]. Structure-based design efforts were fueled by the availability of satisfactory crystallographic structures for eNOS. To date, several eNOS X-ray complexes are documented in the Protein Data Bank (e.g., PDB codes: 3N5P, 3N5Q, 3N56, 3N67, 3N6C, 3NLG, 3E7S, 1RS8, 1RS9[33] and 1P6N with the resolution range of 2.09 to 2.90 Å). However, crystallographic structures are limited by inadequate resolution[35] and ligand–protein complex artifacts[36-38] and ignore the structural heterogeneity related to protein anisotropic motion and discrete conformational substrates [39].

The continued interest in designing new eNOS inhibitors and the lack of adequate ligand-based computer-aided drug discovery efforts combined with the drawbacks of structure-based design prompted us to explore the possibility of developing ligand-based three-dimensional (3D) pharmacophore(s) integrated within a self-consistent QSAR model. This pharmacophore model(s) will then be used as 3D search queries to discover new eNOS inhibitory scaffolds. Our innovative approach was validated previously through the successful discovery of new inhibitory leads scaffolds against glycogen synthase kinase 3β[40], dipeptidyl peptidase[41], hormone sensitive lipase[42], bacterial MurF[43], protein tyrosine phosphatase 1B[44], influenza neuraminidase[45] and cholesteryl ester transfer protein[46], renin[47], peroxisome proliferator-activated receptor gamma[48], β-D-Galactosidase[49], β-D-Glucosidase[50].

A Catalyst-Hypogen module embedded in a Discovery Studio (version 2.5)[51] was employed to construct several logical binding hypotheses for an eNOS inhibitor. Afterward, genetic function algorithm (GFA) and multiple linear regression (MLR) analyses were employed to search for an optimal QSAR that combines high-quality binding pharmacophores with other molecular descriptors and capable of explaining bioactivity variation across a collection of diverse eNOS inhibitors. The optimal pharmacophore was validated by a receiver-operating characteristic (ROC) curve.

RESULTS AND DISCUSSION

The drug receptor model interaction generated by the Hypogen-Catalyst model depends on the ligand structure.[40, 42, 43, 45, 46, 52] Therefore, training molecules chosen varies in bioactivities from 3 to 4 orders of magnitude according to the geometric localization of their chemical features. The Hypogen-Catalyst model identifies a 3D array of a maximum of five chemical features common to active training molecules, which provides a relative alignment for each input molecule consistent with their binding to a proposed common receptor site. The chemical features considered can be hydrogen bond donors and acceptors (HBD and HBA), aliphatic and aromatic hydrophobes (Hbic), positive and negative ionizable (PosIon and NegIon) groups and aromatic planes (RingArom). The conformational flexibility of training ligands is modeled by creating multiple conformers, judiciously prepared to emphasize representative coverage over a specified energy range. Catalyst pharmacophores have been used as 3D queries for mining structural databases for new active leads.[40, 42-46] In the present project, we generated diverse hypotheses for a series of eNOS inhibitors. A total of 151 compounds were used in this study (Table A under Supplementary Material).[28, 53-65] Ten training subsets were selected from the collection (Table B under Supplementary Material). Each subset consisted of inhibitors of wide structural diversity that seem to follow certain common structure-activity rules.

Exploration of eNOS Pharmacophoric Space

The literature was surveyed to collect structurally diverse eNOS inhibitors (1-151, Table A under Supplementary Material).[28, 53-65] The structures were used for conformational analyses. The conformational space of each inhibitor was sampled by a poling algorithm. Subsequently, many pharmacophoric binding modes assumed by eNOS inhibitors were identified (see *Pharmacophoric Hypotheses Generation* in Experimental and Supplementary Materials).[50] The pharmacophoric space of eNOS inhibitors was explored through 64 Hypogen automatic runs and employed ten carefully selected training subsets: subsets I-X in Table B under

Supplementary Material (See *Pharmacophoric Hypotheses Generation* in Experimental and Supplementary Materials). Each training subset complied with certain general 3D SAR rules.

Guided by our rationally restricted pharmacophoric exploration concept, we restricted the software to explore pharmacophoric models incorporating from zero to two PosIon features, from zero to three HBA, from zero to three HBD, and from zero to two Hbic features, as shown in Table C under Supplementary Material. Furthermore, we instructed the Hypogen to explore only 4- and 5-featured pharmacophores (as shown in Table C under Supplementary Material). In each run, the resulting binding hypotheses were automatically ranked according to their corresponding "total cost" value (see *Assessment of the Generated Hypotheses*). An additional validation technique based on Fisher's randomization test [50] was performed (see *Assessment of the Generated Hypotheses*).[51] Eventually, 640 pharmacophore models emerged from 64 automatic Hypogen runs, out of which only 620 models illustrated Cat Scramble confidence levels ≥ 85%. These successful models were clustered and the best representatives (62 models) were used in subsequent QSAR modeling (see *Clustering of the Generated Pharmacophore Hypotheses*). Table 1 shows the statistical criteria of representative cluster centers. Clearly, from the table, representative models shared comparable features and acceptable statistical success criteria. The fact that many pharmacophore models were optimal and statistically comparable suggests the ability of eNOS ligands to assume multiple pharmacophoric binding modes within the binding pocket. Therefore, it is quite challenging to select any particular pharmacophore hypothesis as a sole representative of the binding process.

QSAR Modeling

Pharmacophore modeling of an eNOS inhibitor furnished several binding hypotheses of comparable success criteria which prompted us to employ a classical QSAR analysis to search for the best combination of pharmacophore(s) and other 2D descriptors capable of explaining bioactivity variation across the whole list of collected inhibitors (**1-151**, Table A in Supplementary

Materials). The fit values obtained by mapping representative hypotheses (62 models) against a collected eNOS inhibitor (**1-151**) were enrolled, together with nearly 250 other physicochemical descriptors, as independent variables (genes) in GFA-MLR-QSAR analysis (see *QSAR Modeling*). [40, 42-46]

Interestingly, all our attempts to achieve self-consistent and predictive QSAR models were futile prompting us to evaluate an alternative modeling strategy, namely, to employ ligand efficiency based on heavy atoms (log(Ki)/LEHA) as the response variable instead of activity (log (Ki)). This novel strategy proved successful in achieving self-consistent QSAR models.[66]

However, since it is essential to access the predictive power of the resulting QSAR models on an external set of inhibitors, we randomly selected 30 molecules (marked with double asterisks in Table A, see *QSAR Modeling*) and employed them as external test molecules for validating the QSAR models (r^2_{PRESS}). Moreover, all QSAR models were cross validated automatically using the leave-one-out cross-validation in Discovery Studio 2.5.[51] Eq. (1) shows the details of the optimal QSAR model. Fig. 1 shows the corresponding scatter plots of experimental versus estimated bioactivities for the training and testing inhibitors.

$$\frac{Log(1/Ki)}{LEHA} =$$

$-0.18 + 1.5 \times 10^{-3} (\mathbf{HypoVI/34/1})^2 + 2.29 \times 10^{-3}(JursWPSA3) + 1.08 (Atype H48) - 0.01(Atype H48 \times JursWPSA) - 2.32 \times 10^{-3}[197.2-(JursWPSA3)^2] - 1.17 (Atype H48 \times JursRASA)$

$r^2121 = 0.77$, F-statistic = 63.5, $r^2Adj = 0.76$, $r^2LOO = 0.62$, $r^2PRESS = 0.63$ …..(1)

Where r^2_{121} is the correlation coefficient against 121 training compounds, r_{LOO}^2 is the leave-one-out correlation coefficient, r^2_{adj} is r^2 adjusted for the number of terms in the model and r^2_{PRESS} is the predictive r^2 determined for the 30 test compounds.[51, 67] **HypoVI/34/1** represents the fit values of the training compounds against the first

pharmacophoric hypotheses generated in the 34th Hypogen run employing subset VI (Table B under Supplementary Materials). The fit values were calculated based on Eq. (D) under Supplementary Materials. JursWPSA3 is surface-weighted charged partial surface area calculated by multiplying the total charge weighted positive surface area (determined from the product of partial positive solvent accessible surface area multiplied by the total positive charge) by the total molecular solvent-accessible surface area and dividing by 1000. JursRASA is the relative hydrophobic surface area determined by dividing the total hydrophobic surface area by the total molecular solvent-accessible surface area. AtypeH48 is a member of the thermodynamic AlogP_Atypes family of descriptors and it encodes for the hydrophobic contributions of hydrogen atoms attached to unsaturated centers (i.e., sp^2 or sp hybridized carbon atoms) and geminal to oxygen or nitrogen atoms, usually associated with heterocyclic aromatic rings.[53] Tables D and F under Supplementary Materials show values of QSAR descriptors in equation (1) calculated for training compounds and captured hits, respectively.

Noticeably, one of the descriptors (i.e., JursWPSA3) emerged in equation (1) in spline format. The spline terms employed herein are "truncated power splines" and are denoted by bolded brackets (**( )**). For example, (**f**(x) - a**)** equals zero if the value of (f(x) - a) is negative. Otherwise, it equals (f(x) - a). [51]

Emergence of Hypo**VI/34/1** in equation (1) suggests that this model resembles the binding interactions tying various ligands with eNOS. The bolded row in Table 1 corresponds to the success criteria of **HypoVI/34/1**. Fig. 2 shows **HypoVI/34/1** and how it fits the potent training compound **148** (Ki = 0.35 M) while Table 2 shows the X, Y, and Z coordinates of the pharmacophore.

Emergence of JursWPSA3 in equation (1) illustrates a certain role played by the ligands' positive charges in the binding process. However, the mixed contributions of this descriptor in bioactivity (positive and negative regression slopes) suggest that the ligands' charges play a complex role in binding. On the other hand, the emergence of Jurs-RASA in equation (1) associated with

a negative slope suggests that ligand-eNOS binding is adversely influenced by the ligand's extended hydrophobic surface area. This trend can be explained based on the hydrophilic nature of the binding site of eNOS, in particular, due to the presence of guanidino of ARG252, the carboxylic acid of GLU363 and the two carboxylic acids of heme moiety within the binding site (see Figures 3A and 3B). These groups require the presence of hydrophilic complementary groups in bound ligands to allow effective binding. Moreover, the emergence of AtypeH48 associated with a positive slope suggests that ligands exhibiting alkynes or electron-rich heterocyclic rings, e.g., furans or pyrroles preferably interact with the eNOS catalytic site via π-stacking against the electron-deficient heme aromatic system.

Comparing Pharmacophore Models with Crystallographic Complexes

To further emphasize the validity of our pharmacophore/QSAR modeling approach, we compared the crystallographic structure of a co-crystallized ligand within the eNOS protein (PDB code: 1RS9)[33] with the way it maps **HypoVI/34/1**. Figure 3 compares the chemical structure of the co-crystallized ligand and how it maps **HypoVI/34/1** employing rigid mapping, i.e., fitting the ligand's bound state against the pharmacophore without conformational adjustments. Clearly, mapping the amidic NH of the co-crystallized ligand against the HBD feature in **HypoVI/34/1** (Figure 3C) corresponds to hydrogen bonding interactions tying this NH with the peptidic carbonyl oxygen of SER248 (Figure 3B). Moreover, fitting the amidic carbonyl oxygen of the co-crystallized ligand against the HBA feature in **HypoVI/34/1** (Figure 3C) corresponds to hydrogen bonding interactions tying this carbonyl oxygen with one of the NHs of the guanidine side chain of ARG252. Similarly, mapping the propylene linker of the ligand against a Hbic feature in **HypoVI/34/1** (Figure 3B) corresponds to fitting this moiety into a hydrophobic ring composed of the isopropyl side chain of Val 338, and the ethylene linkers of the two carboxylic acid side chains of the heme ring (Figure 3B) in the co-crystallized complex. Additionally, the fitting of the α carbon of phenylalanine

fragment of the co-crystallized ligand against a second hydrophobic feature in **HypoVI/34/1** (Figure 3B) corresponds to van der Waals' interaction connecting this CH with the aromatic ring of TRP449 (Figure 3A). Finally, fitting the guanidine nucleus of the co-crystallized ligand against the PosIon feature in **HypoVI/34/1** (Figure 3B) seems to correlate nicely with electrostatic attraction tying this group with the carboxylate side chains of the GLU363 (Figure 3A).

It remains to be mentioned that **HypoVI/34/1** points to a limited number of critical interactions required for high ligand-eNOS affinity in each of the binding modes. In contrast, crystallographic complexes reveal many bonding interactions without highlighting critical ones. Incidentally, Figures 3 only show interactions corresponding to pharmacophoric features while other binding interactions were hidden for clarity.

Receiver Operating Characteristic (ROC) Curve Analysis

To further validate the resulting models (both QSAR and pharmacophores), we subjected **HypoVI/34/1** to receiver operating curve (ROC) analysis. In ROC analysis, the ability of a particular pharmacophore model to correctly classify a list of compounds as actives or inactives is indicated by the area under the curve (AUC) of the corresponding ROC as well as other parameters, namely, overall a rate and overall false negative rate (see *Receiver Operating Characteristic (ROC) Curve Analysis* for more details).[50] Table 3 and Fig. 4 show the ROC results of our QSAR-selected pharmacophore. **HypoVI/34/1** illustrated excellent overall performances with ROC-AUC values exceeding 98%.

CONCLUSIONS

Appreciation of the pathological roles of eNOS-derived NO in modulating cancer-related events (angiogenesis, apoptosis, cell cycle, invasion, and metastasis) stimulated our interest in modeling known inhibitors of this target for potential use towards the development of new cancer-preventing treatments. The pharmacophoric space of eNOS inhibitors was explored

via ten diverse sets of inhibitors and using a Catalyst-Hypogen to identify high quality binding model(s). Subsequently, genetic algorithm and multiple linear regression analysis were employed to access an optimal QSAR model capable of explaining eNOS inhibitors bioactivity variation across 151 collected eNOS inhibitors. One pharmacophoric model emerged in the optimal QSAR equation suggesting the existence of one distinct binding mode accessible to ligands within an eNOS binding pocket.

EXPERIMENTAL

Molecular Modeling

Software and Hardware

The following software packages were utilized in the present research.

- CS ChemDraw Ultra 6.0, Cambridge Soft Corp. (www.cambridgesoft.com), USA.

- Discovery Studio 2.5, Accelrys Inc. (www.accelrys.com), USA.

Pharmacophore and QSAR modeling studies were performed using Discovery Studio 2.5 suite from Accelrys Inc. (San Diego, California, www.accelrys.com) installed on installed on a Core 2 Duo Pentium PC.

Data Set

The structures of 151 eNOS inhibitors[1-15] (Table A under Supplementary Material)[28, 53-65] were collected from recently published literature. Even though inhibitors used were collected from different articles, their *in vitro* bioactivities were determined by the same bioassay methodologies. The bioactivities were expressed by their inhibition constant Ki (M). The logarithm of measured Ki (μM) values was used in the three-dimensional quantitative structure activity analysis (3D-QSAR) and thus correlating the data linear to the free energy change.

The inhibitors two-dimensional (2D) chemical structures were sketched using ChemDraw Ultra and saved in MDL-mol file format. Afterward, they were imported into the Catalyst, converted into corresponding standard 3D structures and energy minimized to the closest local minimum using the molecular mechanics

CHARMm force field implemented in the Catalyst. The resulting 3D structures were utilized as starting conformers for the Catalyst conformational analysis.

Conformational Analysis

The molecular flexibilities of the collected compounds were taken into account by considering each compound as a collection of conformers representing different areas of the conformational space accessible to the molecule within a given energy range. Accordingly, the conformational space of each inhibitor (**1-151**, Table A under supplementary material) was explored adopting the "best conformer generation" option within the Catalyst based on the generalized CHARMm force field implemented in the program. Default parameters were employed in the conformation generation procedure of training compounds and screened library (NCI), i.e., a conformational ensemble was generated with an energy threshold of 20 kcal/mol from the local minimized structure at which has the lowest energy level and a maximum limit of 250 conformers per molecule.

Pharmacophoric Hypotheses Generation

All 151 molecules with their associated conformational models were regrouped into a spreadsheet. The biological data of the inhibitors were reported with an "Uncertainty" value of 3, which means that the actual bioactivity of a particular inhibitor is assumed to be situated somewhere in an interval ranging from one-third to three-times the reported bioactivity value of that inhibitor. Subsequently, ten structurally diverse training subsets (sets **I-X** in table B under supplementary material) were carefully selected from the collection for pharmacophore modeling. Typically, the Catalyst requires informative training sets that include at least 16 compounds of evenly spread bioactivities over at least 3.5 logarithmic cycles. Lesser training lists could lead to a chance correlation and thus faulty models.

The selected training sets were utilized to conduct 64 modeling runs to explore the pharmacophoric space of eNOS inhibitors (Table C under supplementary material). The exploration process included altering inter-feature spacing parameter (100 and 300 picometers) and the

maximum number of allowed features in the resulting pharmacophore hypotheses, i.e., they were allowed to vary from 4 to 5 or 5 to 5 with and without exclusion spheres (Table C under supplementary material). Pharmacophore modeling employed the Catalyst proceeds through three successive phases: the constructive phase, subtractive phase and optimization phase.[50]

Assessment of the Generated Hypotheses

When generating hypotheses, the Catalyst attempts to minimize a cost function consisting of three terms: Weight cost, Error cost and Configuration cost.

An additional approach to assess the quality of the Catalyst-Hypogen pharmacophores is to cross-validate them using the Cat-Scramble program implemented in the Catalyst. This validation procedure is based on Fisher's randomization test.[50] In this validation test, we selected a 95% confidence level, which instructed the Catalyst to generate 19 random spreadsheets by the Cat-Scramble command. Subsequently, the Catalyst-Hypogen was challenged to use these random spreadsheets to generate hypotheses using exactly the same features and parameters used in generating the initial unscrambled hypotheses. Success in generating pharmacophores of comparable cost criteria to those produced by the original unscrambled data reduces the confidence in the training compounds and the unscrambled original pharmacophore models.[50, 68] Based on Fisher randomization criteria, only 620 pharmacophores exceeded the 85% significance threshold for subsequent processing (clustering and QSAR analyses).

Clustering of the Generated Pharmacophore Hypotheses

The successful models (620) were clustered into 62 groups (one representative from close sets of 10 models) utilizing the hierarchical average linkage method available in the Catalyst. Subsequently, the highest-ranking representatives, as judged based on their significant F-values, were selected to represent their corresponding clusters in subsequent QSAR modeling. Table 1 shows information about the representative pharmacophores including their pharmacophoric features,

success criteria and differences from corresponding null hypotheses. The table also shows the corresponding Cat-Scramble confidence levels for each representative pharmacophore.

QSAR Modeling

A subset of 121 compounds from the total list of inhibitors (**1-151**, Table A under supplementary material) [28, 53-65] was utilized as a training set for QSAR modeling, and the remaining 30 molecules (*ca.* 20% of the dataset) were employed as an external test subset for validating the QSAR models. The test molecules were selected as follows: the 151 inhibitors were ranked according to their Ki values, and then every fifth compound was selected for the test set starting from the high-potency end. This selection considered that the test molecules must represent a range of biological activities similar to that of the training set. The selected test inhibitors were marked with double asterisks in Table A under supplementary material.

The logarithm of measured ligand efficiency heavy atom (-log (Ki)/LEHA) values was used in QSAR and thus correlating the data linear to the free energy change. The chemical structures of the inhibitors were imported into the Discovery studio as standard 3D single conformer representations in SD format. Subsequently, different descriptor groups were calculated for each compound. The calculated descriptors included various simple and valence connectivity indices, electro-topological state indices and other molecular descriptors (e.g., logarithm of partition coefficient, polarizability, dipole moment, molecular volume, molecular weight, molecular surface area, etc.).[51] The training compounds were fitted (using the best-fit option in the Catalyst module of the Discovery studio)[51] against the representative pharmacophores (121 models, Table 1), and their fit values were added as additional descriptors. The fit value for any compound was obtained automatically via equation (5).[51]

Genetic function approximation (GFA) was employed to search for the best possible QSAR regression equation capable of correlating the variations in biological activities of the training compounds with variations in the generated

descriptors, i.e., multiple linear regression modeling (MLR). GFA techniques rely on the evolutionary operations of ''crossover and mutation'' to select optimal combinations of descriptors (i.e., chromosomes) capable of explaining bioactivity variation among training compounds from a large pool of possible descriptor combinations, i.e., chromosomes population. However, to avoid overwhelming GFA-MLR with a large number of poor descriptor populations, we removed lowest-variance descriptors (20%) prior to QSAR analysis.

Each chromosome was associated with a fitness value that reflected how good it was when compared to other solutions. The fitness function employed herein is based on Friedman's 'lack-of-fit' (LOF).[51]

Our preliminary diagnostic trials suggested the following optimal GFA parameters: explore linear, quadratic and spline equations at mating and mutation probabilities of 50%, population size = 500, number of genetic iterations = 30,000 and lack-of-fit (LOF) smoothness parameter = 1.0. However, to determine the optimal number of explanatory terms (QSAR descriptors), it was decided to scan and evaluate all possible QSAR models resulting from 4 to 10 explanatory terms.

All QSAR models were validated employing leave one-out cross-validation (r^2_{LOO}), adjusted (r^2_{adj}) and predictive r^2 (r^2_{PRESS}) calculated from the test subsets. The predictive r^2_{PRESS} was defined as in equation 2:

$$r^2_{PRESS} = SD\text{-}PRESS/SD \quad \ldots\ldots\ldots\ldots\ldots\ldots\ldots\ldots (2)$$

Where SD is the sum of the squared deviations between the biological activities of the test set and the mean activity of the training set molecules, and PRESS is the squared deviations between the predicted and actual activity values for every molecule in the test set.

Receiver Operating Characteristic (ROC) Curve Analysis

The selected pharmacophore models (i.e., **HypoVI/34/1**) were validated by assessing their abilities

to selectively capture diverse eNOS active compounds from a large testing list of actives and decoys.

The testing list was prepared as described by Verdonk and co-workers.[69, 70] Briefly, decoy compounds were selected based on three basic one-dimensional (1D) properties that allow the assessment of distance (D) between two molecules (e.g., i and j): (1) the number of hydrogen-bond donors (NumHBD), (2) number of hydrogen-bond acceptors (NumHBA) and (3) count of nonpolar atoms (NP, defined as the summation of Cl, F, Br, I, S and C atoms in a particular molecule). For each active compound in the test set, the distance to the nearest other active compound was assessed by their Euclidean Distance (Eq. (3)):

$$D(i,j) = \sqrt{\begin{array}{l}(NumHBD_i - NumHBD_j)^2 + \\ (NumHBA_i - NumHBA_j)^2 + (NP_i - NP_j)^2\end{array}} \quad (3)$$

The minimum distances are then averaged over all active compounds (Dmin). Subsequently, for each active compound in the test set, around 36 decoys were randomly chosen from the ZINC database. The decoys were selected in such a way that they did not exceed Dmin distance from their corresponding active compound.

To diversify active members in the list, we excluded any active compound having zero distance ($D(i,j)$) from other active compound(s) in the test set. Active testing compounds were defined as those possessing eNOS affinities ranging from 0.35 to 700 μM. The test set included 22 active compounds and 731 ZINC decoys.

The test set (753 compounds) was screened by each particular pharmacophore employing the "Best flexible search" option implemented in the Catalyst, while the conformational spaces of the compounds were generated employing the "Fast conformation generation option" implemented in the Catalyst. Compounds missing one or more features were discarded from the hit list. *In-silico* hits were scored employing their fit values as calculated by Eq. (D) in the Supplementary Materials.

The ROC curve analysis describes the sensitivity (Se or true positive rate, Eq. (4)) for any possible change in the

number of selected compounds (n) as a function of (1-Sp). Sp is defined as specificity or true negative rate (Eq. (5)).[50]

$$Se = \frac{Number\ of\ Selected\ Actives}{Total\ Number\ of\ Actives} = \frac{TP}{TP+FN} \quad \ldots\ldots(4)$$

$$Sp = \frac{Number\ of\ Discarded\ Inactives}{Total\ Number\ of\ Inactives} = \frac{TN}{TN+FP} \ldots\ldots(5)$$

Where, TP is the number of active compounds captured by the virtual screening method (true positives), FN is the number of active compounds discarded by the virtual screening method, TN is the number of discarded decoys (presumably inactives),[50] while FP is the number of captured decoys (presumably inactive). If all molecules scored by a virtual screening (VS) protocol with sufficient discriminatory power are ranked according to their score (i.e., fit values), starting with the best-scored molecule and ending with the molecule that got the lowest score, most of the actives will have a higher score than the decoys. Since some of the actives will be scored lower than decoys, an overlap between the distribution of active molecules and decoys will occur, which will lead to the prediction of false positives and false negatives. The selection of one score value as a threshold strongly influences the ratio of actives to decoys and therefore the validation of a VS method. The ROC curve method avoids the selection of a threshold by considering all Se and Sp pairs for each score threshold.

A ROC curve was plotted by setting the score of the active molecule as the first threshold. Afterwards, the number of decoys within this cutoff was counted and the corresponding Se and Sp pair was calculated.[50] This calculation was repeated for the active molecule with the second highest score and so forth, until the scores of all actives were considered as selection thresholds.

The ROC curve representing ideal distributions, where no overlap between the scores of active molecules and decoys exists, proceeds from the origin to the upper-left corner until all the actives are retrieved and Se reaches the value of 1. In contrast to that, the ROC curve

for a set of actives and decoys with randomly distributed scores tends towards the Se = 1-Sp line asymptotically with increasing number of actives and decoys.[50] The success of a particular virtual screening workflow can be judged from the following criteria (shown in Table 3):

1)   In an optimal ROC curve, the value of the area under the ROC curve (AUC)[50] of 1 is obtained. However, random distributions cause an AUC value of 0.5. Virtual screening that performs better than a random discrimination of actives and decoys retrieve an AUC value between 0.5 and 1, whereas an AUC value lower than 0.5 represents the unfavorable case of a virtual screening method that has a higher probability to assign the best scores to decoys than to actives.

2)   Overall Accuracy (ACC) describes the percentage of correctly classified molecules by the screening protocol (Eq. (6)). Testing compounds are assigned a binary score value of zero (compound not captured) or one (compound captured).[50]

$$ACC = \frac{TP+TN}{N} = \frac{A}{N}.Se + \left(1 - \frac{A}{N}\right).Sp \quad \ldots\ldots(6)$$

where N is the total number of compounds in the testing database, and A is the number of true actives in the testing database.

3)   Overall specificity (SPC) describes the percentage of discarded inactives by the particular virtual screening workflow. Inactive test compounds are assigned a binary score value of zero (compound not captured) or one (compound captured) regardless of their individual fit values.[50]

4)   Overall True Positive Rate (TPR or overall sensitivity) describes the fraction percentage of captured actives from the total number of actives. Active test compounds are assigned a binary score value of zero (compound not captured) or one (compound captured) regardless of their individual fit values.[50]

5)   Overall False Negative Rate (FNR or overall percentage of discarded actives) describes the fraction percentage of active compounds discarded by the virtual screening method. Discarded active test compounds are

assigned a binary score value of zero (compound not captured) or one (compound captured) regardless to their individual fit values.[50]
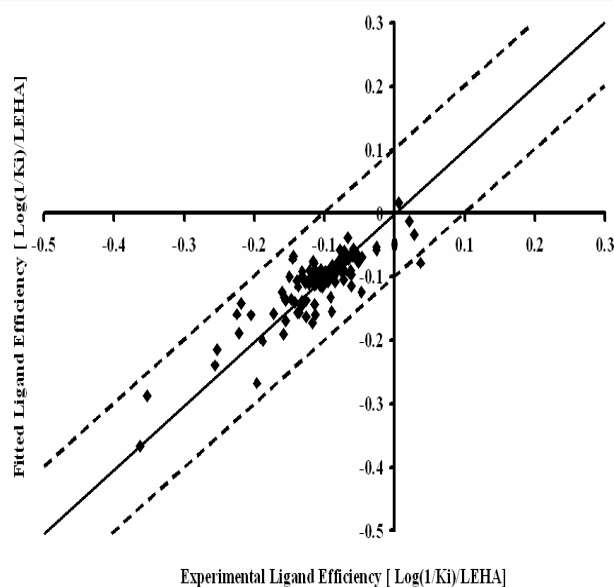
In Silico Screening for New eNOS Inhibitors

The **HypoVI/34/1** was employed as 3D search queries to screen the NCI 3D flexible structural databases. The screening was done employing the "Best Flexible Database Search" option implemented within the Catalyst. Hits were filtered according to Lipinski's[71] and Veber's rules[72] (Table 4). Remaining hits were fitted
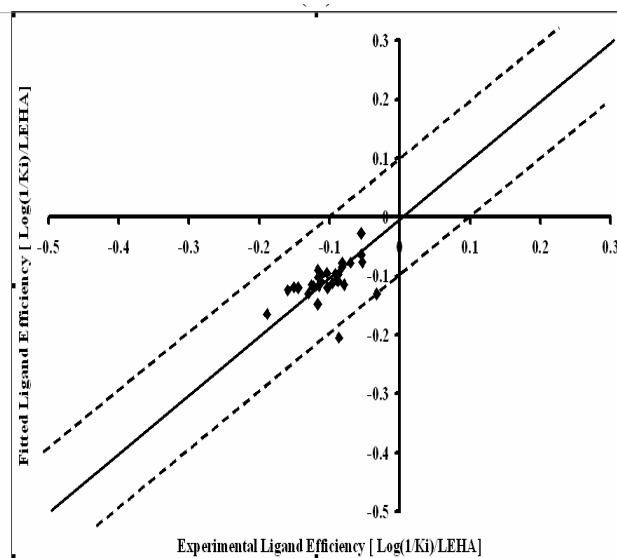
against the one pharmacophore using the "best fit" option within the Catalyst. The fit value with the relevant molecular descriptors of each hit was substituted in the optimal QSAR equation (1). Table 5 shows active hits and their QSAR-predictions.

ACKNOWLEDGMENTS

(A)

(B)

Figure 1: Experimental versus (A) fitted (121 compounds, $r2_{LOO}$= 0.62), and (B) predicted (30 compounds, $r2_{PRESS}$= 0.63) bioactivities calculated from the best QSAR model equation (1). The solid lines are the regression lines for the fitted and predicted bioactivities of training and test compounds, respectively, whereas the dotted lines indicate 0.1 log point error margins.
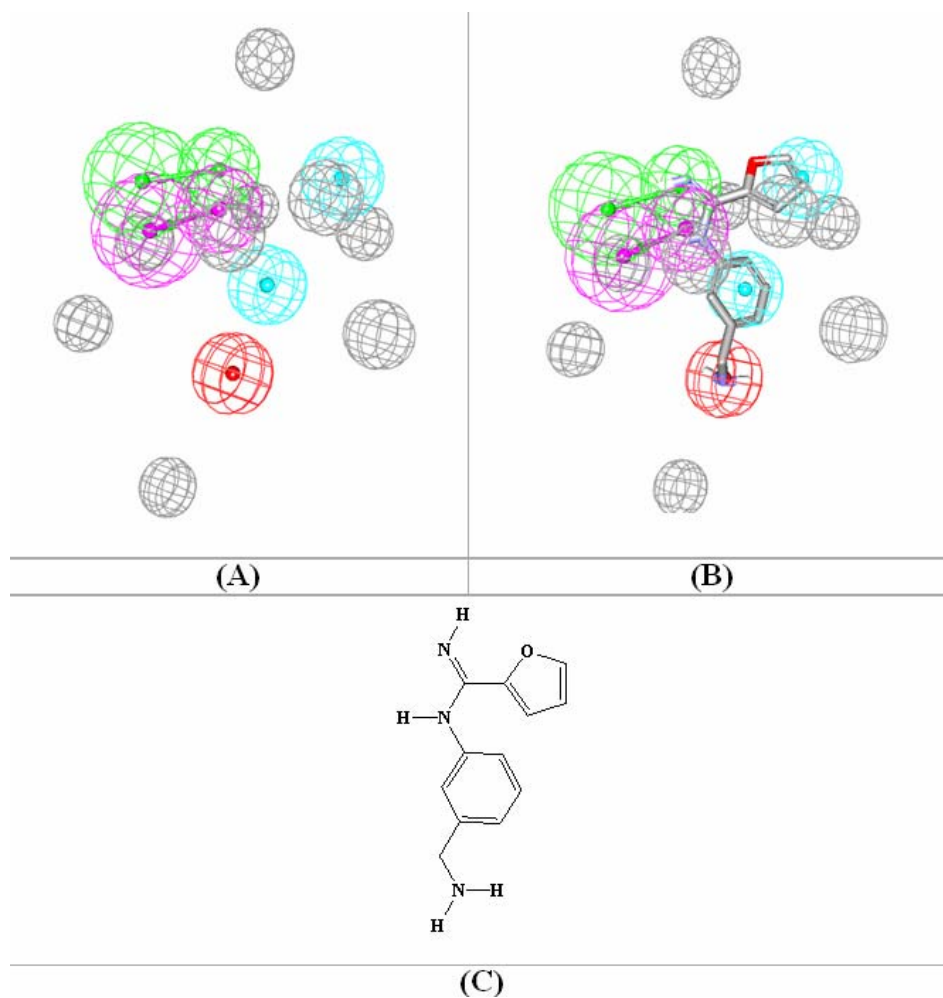
Figure 2: (A) Pharmacophoric features of HypoVI/34/1. HBA as green vectored spheres, HBD as pink vectored spheres, Hbic as blue spheres, PosIon as red spheres (B) HypoVI/34/1 fitted against 148 (Ki = 0.35 M, Table A under Supplementary Materials), (C) Chemical structure of 148
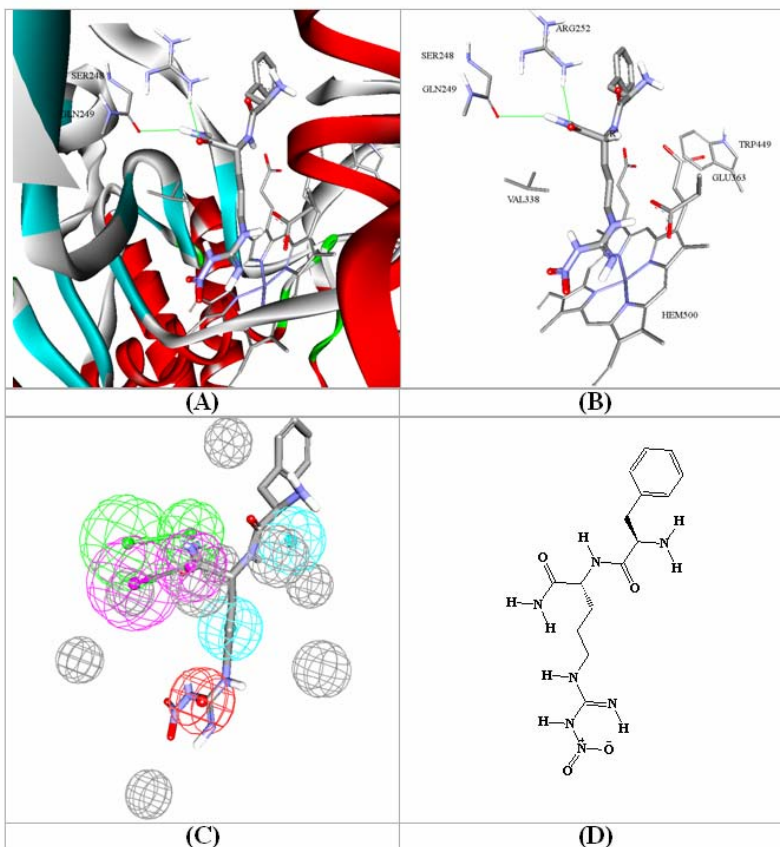
Figure 3: (A), (B) Co-crystallized ligand of eNOS (PDB code: 1RS9, resolution 2.22 Ǻ), (C) HypoVI/34/1 mapped against the co-crystallized ligand of 1RS9 (D) the chemical structure of the co-crystallized ligand of 1RS9.
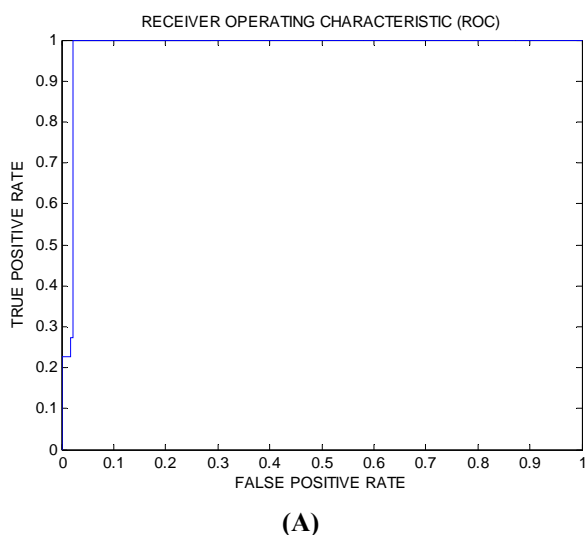

(A)

Figure 4: ROC curves of: (A) HypoVI/34/1.

Table 1: The performance of best representatives of clustered pharmacophore hypotheses generated for eNOS.

Training set	Hypotheses[a]	Pharmacophoric features in generated hypotheses	Total cost	Cost of null hypotheses	Residual cost[b]	Conf.cost[c]	R[d]	F/statistic[e]	Cat. scramble%
	HypoI/1/10[f]	Hbic, HBA, 2×HBD	119.15	150.50	31.35	12.94	0.83	0.003	95
	HypoI/3/8	2×Hbic, 2×HBD, PosIon	119.45	150.50	31.05	9.49	0.81	0.001	95
I	HypoI/5/1	2×Hbic, HBA, HBD, 8EV	103.74	150.50	46.76	12.94	0.96	21.623	95
	HypoI/5/7	Hbic, HBA, HBD, PosIon,1EV	118.61	150.50	31.89	12.94	0.83	3.346	95
	HypoI/5/8	Hbic, 2×HBA, HBD, 1EV	118.98	150.50	31.52	12.94	0.83	0.261	95
	HypoI/6/1	2×Hbic, HBA, PosIon, 9EV	102.75	150.50	47.75	11.26	0.95	17.132	95
	HypoII/8/4	2×Hbic, 2×PosIon	121.62	157.64	36.02	11.26	0.88	8.262	95
	HypoII/8/8	2×Hbic, HBA, PosIon	122.95	157.64	34.69	11.26	0.86	6.692	95
II	HypoII/12/7	Hbic, 2×HBA, HBD, 4EV	120.26	157.64	37.38	11.26	0.89	1.740	95
	HypoII/10/1	2×Hbic, HBA, HBD, PosIon,6EV	113.14	157.64	44.50	9.49	0.93	19.006	95
	HypoII/10/4	2×Hbic, 2×HBD, PosIon	119.23	157.64	38.41	9.49	0.88	11.557	95
	HypoII/14/10	2×Hbic, HBD, PosIon	116.45	157.04	40.59	11.26	0.85	9.740	95
	HypoIII/15/7	2×Hbic, 2×HBD, PosIon	112.37	157.04	44.67	9.49	0.87	12.561	95
	HypoIII/17/1	2×Hbic, HBA, HBD, PosIon, 5EV	104.67	157.04	52.37	12.94	0.96	15.259	95
III	HypoIII/17/6	2×Hbic, HBA, PosIon, 6EV	114.15	157.04	42.89	12.94	0.89	12.415	95
	HypoIII/17/10	Hbic, HBA, 2×HBD, 1EV	117.45	157.04	39.59	12.94	0.86	2.922	95
	HypoIII/18/7	2×Hbic, HBA, HBD, 3EV	111.98	157.04	45.07	11.26	0.89	17.270	95
	HypoIV/19/1	Hbic, HBA, 2×HBD	96.83	132.34	35.51	12.80	0.90	1.472	95
	HypoIV/20/2	2×Hbic, HBA, HBD	97.05	132.34	35.30	11.04	0.88	12.777	95
IV	HypoIV/23/1	Hbic, HBA, HBD, PosIon, 9EV	93.68	132.34	38.66	12.94	0.93	2.962	90
	HypoIV/23/2	Hbic, 2×HBA, HBD, 9EV	94.02	132.34	38.32	12.94	0.93	3.080	95
	HypoIV/23/6	HBA, HBD, 2×PosIon, 3EV	100.17	132.34	32.17	12.94	0.87	1.456	95
	HypoIV/24/8	2×Hbic, HBA, PosIon, 1EV	99.06	132.34	33.28	11.26	0.86	7.262	95
	HypoV/26/3	2×Hbic, 2×PosIon	97.69	128.63	30.94	11.26	0.92	7.939	95
	HypoIV/27/10	2×Hbic, HBA, 2×PosIon	100.98	128.63	27.65	9.50	0.87	0.358	95
V	HypoIV/29/3	Hbic, HBA, 2×HBD, 2EV	99.10	128.63	29.53	12.94	0.92	2.473	95
	HypoIV/29/7	2×Hbic, HBA, HBD, 1EV	99.43	128.63	29.20	12.94	0.92	13.151	95
	HypoIV/30/4	2×Hbic, 2×HBD	96.89	128.63	31.74	11.26	0.93	10.217	95
	HypoIV/30/5	2×Hbic, HBD, PosIon	97.13	128.63	31.51	11.26	0.93	7.788	95

[a] High ranking representative hypotheses (in their corresponding clusters, see section 4.1.6). [b] Difference between total cost and the cost of the corresponding null hypotheses. [c] Conf.cost, [d] Correlation coefficients between pharmacophore/based bioactivity estimates and bioactivities of corresponding training compound (subsets in table B under supplementary material). [e] Fisher statistic calculated based on the linear regression between the fit values of all collected inhibitors (**1/151**, table A under supplementary material) against pharmacophore hypothesis (employing the "best fit" option and equation (D) and their respective eNOS inhibitory activity (log (1/Ki) values). [f] Models names encode for the training sets, run numbers and model rank in each run, e.g., HypoI/1/10 encode for the 10rd pharmacophore model generated from training subset **I** (Table B under Supplementary Materials) in run number 1 (Table C under Supplementary Materials). [g] Bolded pharmacophores appeared in the best QSAR equations.

Table 1: The performance of best representatives of clustered pharmacophore hypotheses generated for eNOS.

Training set	Hypotheses[a]	Pharmacophoric features in generated hypotheses	Total cost	Cost of null hyptheses	Resdiual cost[b]	Conf.cost[c]	R[d]	F/statistic[e]	Cat. scramble%
	HypoVI/31/3[f]	Hbic, HBA, 2×HBD	112.37	140.45	28.08	12.94	0.89	8.237	95
	HypoVI/32/2	2×Hbic, HBA, HBD	109.86	140.45	30.58	11.26	0.90	11.589	95
	HypoVI/32/6	2×Hbic, 2×PosIon	111.03	140.45	29.42	11.26	0.89	4.239	95
VI	**HypoVI/34/1[g]**	**2×Hbic, HBA, HBD, PosIon, 9EV**	**104.87**	**140.45**	**35.58**	**9.50**	**0.93**	**21.100**	**90**
	HypoVI/35/1	2×Hbic, HBA, PosIon, 8EV	105.92	140.45	34.53	12.94	0.96	19.398	95
	HypoVI/35/10	2×Hbic, 2×HBD	113.32	140.45	27.13	12.94	0.88	12.895	95
VII	HypoVII/37/5	Hbic, 2×HBA, PosIon	104.84	121.19	16.35	17.68	0.91	0.055	95
	HypoVII/37/6	Hbic, 3×HBA	106.67	121.19	14.52	17.68	0.89	0.000	95
	HypoVII/38/5	Hbic, 2×HBA, HBD	102.12	121.19	19.07	15.64	0.90	1.992	95
	HypoVII/39/1	2×Hbic, 2×HBA, PosIon	97.28	121.19	23.91	13.19	0.93	9.794	95
	HypoVII/41/1	Hbic, 2×HBA, HBD	102.82	121.19	18.37	17.68	0.92	0.001	95
VII-10	HypoVII/42/3	Hbic, 2×HBA, PosIon	103.33	121.19	17.86	15.64	0.89	0.668	95
	HypoVIII/43/5	2×Hbic, 2×HBA, PosIon	103.92	121.19	17.27	13.19	0.86	8.265	95
	HypoVIII/43/9	2×Hbic, HBA, HBD, PosIon	104.14	121.19	17.04	13.19	0.85	16.617	95
	HypoVIII/48/4	2×Hbic, 2×HBD, PosIon	106.51	141.18	34.67	9.49	0.85	11.112	95
VIII	HypoVIII/49/4	2×Hbic, HBA, HBD, PosIon, 5EV	102.03	141.18	39.15	12.94	0.91	23.349	95
	HypoVIII/49/5	2×Hbic, HBA, HBD, 6EV	99.79	141.18	41.39	12.94	0.94	10.063	95
	HypoVIII/50/2	2×Hbic, HBA, PosIon, 8EV	94.74	141.18	46.44	11.26	0.96	0.010	95
	HypoVIII/50/6	2×Hbic, 2×HBD	101.85	141.18	39.33	11.26	0.91	9.250	95
	HypoVIII/50/7	2×Hbic, HBA, HBD, 5EV	102.57	141.18	38.62	11.26	0.90	12.045	95
XI	HypoXI/52/9	Hbic, HBA, HBD, PosIon	104.06	126.20	22.14	11.26	0.85	0.162	95
	HypoXI/54/1	2×Hbic, HBA, HBD, PosIon, 7EV	93.63	126.20	32.56	9.50	0.95	2.982	90
	HypoXI/54/6	2×Hbic, 2×HBA, PosIon, 7EV	106.76	126.20	19.44	9.50	0.79	4.412	95

	Model	Features							
	Hypo**XI**/54/8	2×Hbic, HBA, 2×PosIon, 1EV	108.90	126.20	17.29	9.50	0.77	0.339	95
	Hypo**XI**/55/8	Hbic, HBA, 2×HBD, 5EV	103.25	126.20	22.95	12.94	0.87	4.144	95
X	Hypo**X**/57/1	Hbic, 2×HBA, HBD	111.38	125.98	14.60	17.81	0.90	0.524	95
	Hypo**X**/57/5	Hbic, HBA, 2×HBD	112.78	125.98	13.20	17.81	0.88	1.215	95
	Hypo**X**/58/1	Hbic, 2×HBA, HBD	108.44	125.98	17.54	15.65	0.91	2.097	95
	Hypo**X**/58/3	2×Hbic, HBA, HBD	108.75	125.98	17.23	15.65	0.90	4.943	95
	Hypo**X**/1/10	2×Hbic, 2×HBA	114.54	125.98	11.44	17.81	0.85	1.010	95
	Hypo**X**/62/7	Hbic, 2×HBA, PosIon	111.55	125.98	14.43	15.65	0.87	0.038	95
	Hypo**X**/63/4	2×Hbic, 2×HBA, PosIon	107.26	125.98	18.72	14.12	0.91	27.346	95
	Hypo**X**/63/5	2×Hbic, HBA, HBD, PosIon	110.12	125.98	15.86	14.12	0.87	19.781	95

[a]High ranking representative hypotheses (in their corresponding clusters, see *Clustering of the Generated Pharmacophore Hypotheses*

[b]Difference between total cost and the cost of the corresponding null hypotheses. [c]Conf.cost, [d]Correlation coefficients between pharmacophore/based bioactivity estimates and bioactivities of corresponding training compound (subsets in Table B under Supplementary Material). [e]Fisher statistic calculated based on the linear regression between the fit values of all collected inhibitors (**1/151**, Table A under Supplementary Material) against pharmacophore hypothesis (employing the "best fit" option and equation (D) and their respective eNOS inhibitory activity (log (1/Ki) values). [f]Models' names encode for the training sets, run numbers and model rank in each run, e.g., Hypo**I**/1/10 encode for the 10rd pharmacophore model generated from training subset **I** (Table B under Supplementary Materials) in run number 1 (Table C under Supplementary Materials). [g]Bolded pharmacophores appeared in the best QSAR equations.

Table 2: Pharmacophoric features, corresponding tolerances and 3D coordinates (X, Y, Z) of optimal eNOS based pharmacophore models.

Model[a]	definitions		Chemical Features						
			HBA[c] 2.00566		**HBD**[d] 2.00566		**Hbic**[e] 2.00566	**Hbic** 2.00566	**PosIons**[f] 2.00566
	Weights								
Hypo34/1[a]	Tolerances[b]		1.60	2.20	1.60	2.20	1.60	1.60	1.60
	Coordinates	X	-1.68	-0.15	0.18	1.46	-3.02	1.61	5.33
		Y	0.48	2.10	-0.88	1.80	-2.69	-0.64	-0.35
		Z	-2.16	-4.14	-2.51	-3.17	1.15	1.30	1.44

[a]Pharmacophoric hypothesis shown in Figure 2 and Figures 3 . [b]Tolerances: refer to the radius of feature spheres (Å).[c] HBA: Hydrogen Bond Acceptor feature. [d]HBD: Hydrogen Bond Donor feature, Hbic[e]: Hydrophobic feature. [f] PosIons: Positive ionizabile. [f]HBA: Hydrogen Bond Acceptor feature. [g]Number of exclusion spheres in **HypoVI/34/1**= 10 of 1.2 Å tolerance, at the following X,Y, Z coordinates: (1.42 , -2.56 , -3.02), (-2.17 , -2.13 , 4.23), (1.58 , 3.12 , -2.39), (5.48 , 5.15 , -2.37), (-6.77 , 0.40 , -2.10), (10.51 , 2.20 , 2.60), (2.58 , -5.72 , 2.09), (-0.55 , -5.00 , -1.88), (-2.82 , 3.85 , 3.12).

Table 3: Performance of QSAR-selected pharmacophores as 3D search queries.

Pharmacophore Model	ROC[a]- AUC[b]	ACC[c]	SPC[d]	TPR[e]	FNR[f]
HypoVI/34/1	0.98	0.96	0.99	0.27	0.01

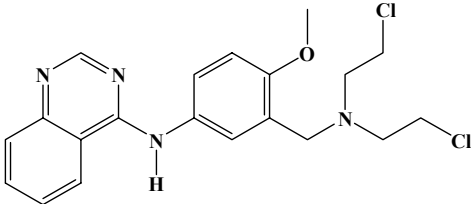[a]**ROC**: Receiver operating characteristic.
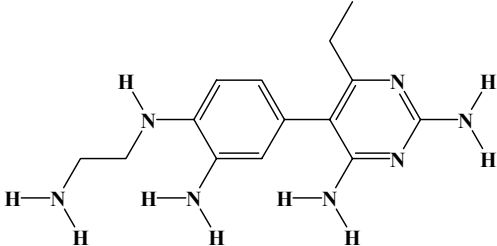[b]**AUC**: Area under the curve.
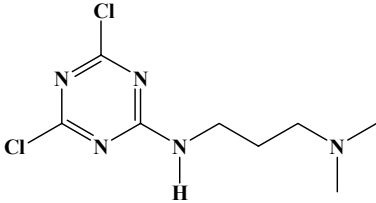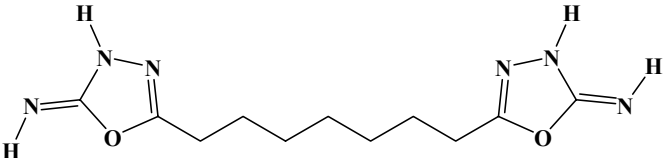[c]**ACC**: Overall accuracy.
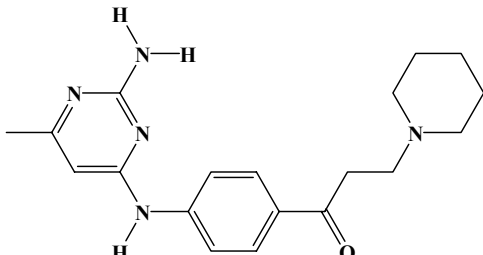[d]**SPC**: Overall specificity.
[e] **TPR**: Overall true positive rate. [f] **FNR**: Overall false negative rate.

Table 4: The number of captured compounds by each pharmacophore model.

3D Database	ost screening filtering[b]	Pharmacophore models HypoVI/34/1
NCI[a]	Before	4100
	After	1351

Table 5: High-ranking hit molecules with their fit values against HypoVI/34/1 and their corresponding QSAR estimates from equation (1).

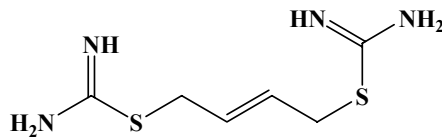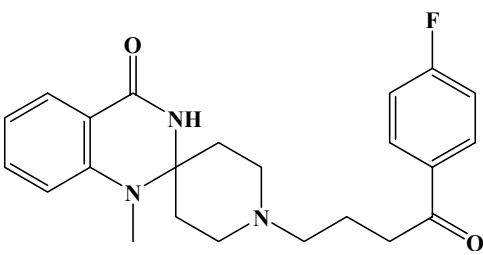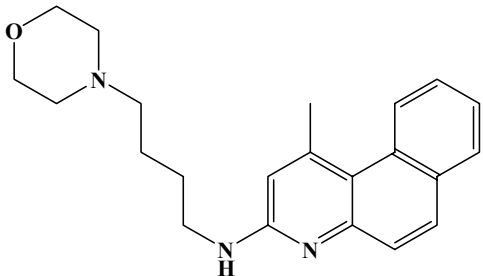| No.[a]	Name	Structure	Fit values[b] HypoVI/34/1	QSAR Predictions[c] Ki (μM)
152	NCI0225379		8.16	0.50
153	NCI0382039		7.47	1.00
154	NCI0231540		7.32	0.66
155	NCI0382943		6.98	0.85

156	NCI0602251		6.96	1.00

aCompound numbers.
bBest- fit values calculated by equation (D) in section SM-1 under Supplementary Materials.
cPredictions based on optimal QSAR model (1).

Table 5: High-ranking hit molecules with their fit values against HypoVI/34/1 and their corresponding QSAR estimates from equation (1).

No.[a]	Name	Structure	Fit values[b]	QSAR Predictions[c]
			HypoVI/34/1	Ki (µM)
170	NCI0014523		5.62	1.00
171	NCI0665292		6.56	0.02
172	NCI0349071		6.40	1.24

173	NCI0507481		6.23	1.24
174	NCI0528635		8.16	0.90

[a]Compound numbers.
[b]Best- fit values calculated by equation (D) in section SM-1 under Supplementary Materials.
[c]Predictions based on optimal QSAR model (1).

REFERENCES

(1)   Liu Z. Q., Wildhirt S. M. and Zhou H. H. Specificity of inducible nitric-oxide synthase inhibitors: prospects for their clinical therapy. *Acta. Pharm. Sinic.* 1999; 20:1052-1056.

(2)   Moncada S., Higgs A. and Furchgott R. International Union of Pharmacology Nomenclature in Nitric Oxide Research. *Pharmacol. Rev.* 1997; 49:137-142.

(3) Bredt D. S. and Snyder S. H. Nitric-oxide - a physiological messenger molecule. *Annu. Rev. Biochem.* 1994; 63:175-195.

(4) Furchgott R. F. and Zawadzki J. V. The Obligatory Role Of Endothelial-Cells In The Relaxation Of Arterial Smooth-Muscle By Acetylcholine. *Nature* 1980; 288:373-376.

(5) Ignarro L. J., Buga G. M., Wood K. S., Byrns R. E. and Chaudhuri G. Endothelium-derived relaxing factor produced and released from artery and vein is nitric-oxide. *P. Natl. Acad. Sci. USA*. 1987: 84:9265-9269.

(6) Palmer R. M. J., Ferrige A. G. and Moncada S. Nitric-oxide release accounts for the biological-activity of endothelium-derived relaxing factor. *Nature* 1987; 327:524-526.

(7) Groves J. T. and Wang C. C. Y. Nitric oxide synthase: models and mechanisms. *Curr. Opin. Chem. Biol.* 2000; 4:687-695.

(8) Aktan F. iNOS-mediated nitric oxide production and its regulation. *Life Sci.* 2004; 75:639-653.

(9) Tousoulis D., Briasoulis A., Papageorgiou N., Tsioufis, C. Tsiamis E., Toutouzas K. and Stefanadis, C. Oxidative stress and endothelial function: therapeutic interventions. *Recent. Pat. Cardiovasc. Drug. Discov.* 2011; 6:103-14.

(10) Ying L. and Hofseth L. J. An emerging role for endothelial nitric oxide synthase in chronic inflammation and cancer. *Cancer Res.* 2007; 67:1407-1410.

(11) Wang L., Shi G. G., Yao J. C., Gong W., Wei D., Wu T. T., Ajani J. A., Huang S. and Xie K. Expression of endothelial nitric oxide synthase correlates with the angiogenic phenotype of and predicts poor prognosis in human gastric cancer. *Gastric. Cancer* 2005; 8:18-28.

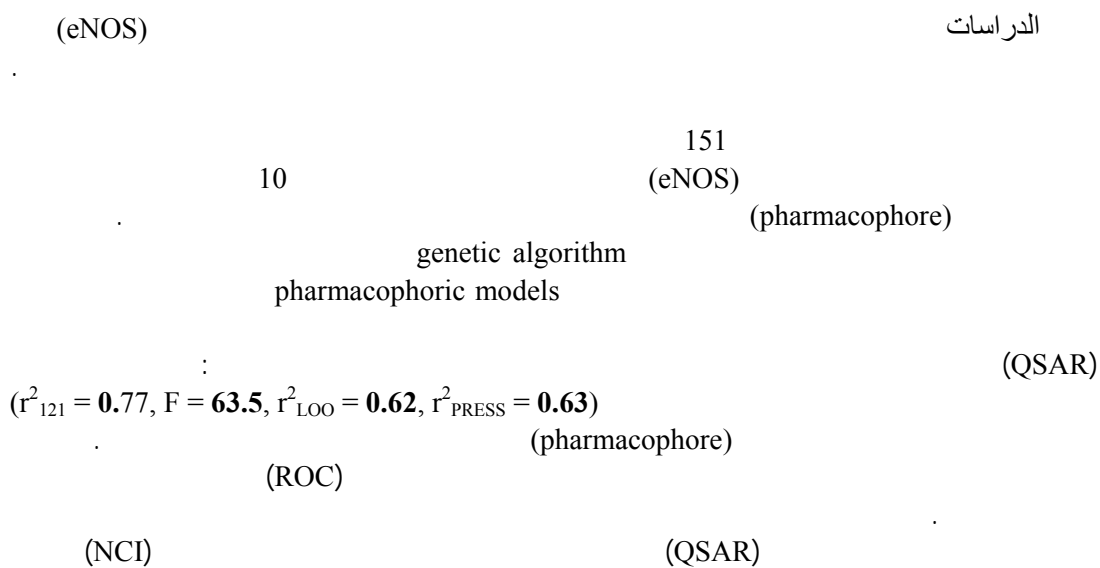(12) Ariel I., Hochberg A. and Shochina M. Endothelial nitric oxide synthase immunoreactivity in early

gestation and in trophoblastic disease. *J. Clin. Pathol.* 1998; 51:427-31.

(13) Calabrese V., Mancuso C., Calvani M., Rizzarelli E., Butterfield D. A. and Stella A. M. G. Nitric oxide in the central nervous system: neuroprotection versus neurotoxicity. *Nat. Rev. Neurosci.* 2007; 8:766-775.

(14) Kroncke K. D., Fehsel K. and Kolb-Bachofen, V. Inducible nitric oxide synthase in human diseases. *Clin. Exp. Immunol.* 1998; 113:147-156.

(15) Ma Q., Wang Z., Zhang M., Hu H., Li J., Zhang D., Guo K. and Sha, H. Targeting the L-arginine-nitric oxide pathway for cancer treatment. *Curr. Pharm. Des.* 2010; 16:392-410.

(16) Wang G. Y., Ji B., Wang X. and Gu J. H. Anti-cancer effect of iNOS inhibitor and its correlation with angiogenesis in gastric cancer. *World J. Gastroenterol.* 2005; 11:3830-3.

(17) Knowles R. G., Palacios M., Palmer R. M. J. and Moncada, S. Formation of nitric-oxide from l-arginine in the central nervous-system - a transduction mechanism for stimulation of the soluble guanylate-cyclase. *P. Natl. Acad. Sci. USA.* 1989: 86:5159-5162.

(18) Rees D. D., Palmer R. M. J., Schulz R., Hodson H. F. and Moncada S., Characterization of 3 inhibitors of endothelial nitric-oxide synthase invitro and invivo. *Brit. J. Pharmacol.* 1990: 101:746-752.

(19) Narayanan K., Spack L., McMillan K., Kilbourn R. G., Hayward M. A., Masters B. S. S. and Griffith O. W. *S*-alkyl-l-thiocitrullines - potent stereoselective inhibitors of nitric-oxide synthase with strong pressor activity in-vivo. *J. Biol. Chem.* 1995; 270:11103-11110.

(20) Naka M., Nanbu T., Kobayashi K., Kamanaka Y., Komeno M., Yanase R., Fukutomi T., Fujimura S., Seo H. G., Fujiwara N., Ohuchida S., Suzuki K., Kondo K. and Taniguchi N. A potent inhibitor of inducible nitric oxide synthase, ONO-1714, a cyclic amidine derivative. *Biochem. Bioph. Res. Co* 2000; 270:663-667.

(21) Wolff D. J. and Lubeskie A. Aminoguanidine is an isoform-selective, mechanism-based inactivator of nitric-oxide synthase. *Arch. Biochem. Biophys.* 1995; 316:290-301.

(22) Kontogiorgis C. A. and Hadjipavlou-Litina D. Current

trends in QSAR on NO donors and inhibitors of nitric oxide synthase (NOS). *Med. Res. Rev.* 2002; 22:385-418.

(23) Vallance P. Nitric oxide: therapeutic opportunities. *Fund. Clin. Pharmacol.* 2003; 17, 1:1-10.

(24) Raman C. S., Li H. Y., Martasek P., Kral V., Masters B. S. S. and Poulos T. L. Crystal structure of constitutive endothelial nitric oxide synthase: A paradigm for pterin function involving a novel metal center. *Cell* 1998; 95:939-950.

(25) Aparna V., Desiraju G. R. and Gopalakrishnan B. Insights into ligand selectivity in nitric oxide synthase isoforms: A molecular dynamics study. *J. Mol. Graph. Model.* 2007; 26:457-470.

(26) Crane B. R., Arvai A. S., Gachhui R., Wu C. Q., Ghosh D. K., Getzoff E. D., Stuehr D. J. and Tainer, J. A. The structure of nitric oxide synthase oxygenase domain and inhibitor complexes. *Science* 1997; 278:425-431.

(27) Ji H., Gómez-Vidal J. A., Martásek P., Roman L. J. and Silverman R. B. Conformationally Restricted Dipeptide Amides as Potent and Selective Neuronal Nitric Oxide Synthase Inhibitors. *J. Med. Chem.* 2006; 49:6254-6263.

(28) Seo J., Martasek P., Roman L. J. and Silverman R. B. Selective L-nitroargininylaminopyrrolidine and L-nitroargininylaminopiperidine neuronal nitric oxide synthase inhibitors. *Bioorgan. Med. Chem.* 2007; 15:1928-1938.

(29) Davey D. D., Adler M., Arnaiz D., Eagen K., Erickson S., Guilford W., Kenrick M., Morrissey M. M., Ohlmeyer M., Pan G., Paradkar V. M., Parkinson J., Polokoff M., Saionz K., Santos C., Subramanyam B., Vergona R., Wei R. G., Whitlow M., Ye B., Zhao Z., Devlin J. J. and Phillips G. Design, Synthesis, and Activity of 2-Imidazol-1-ylpyrimidine Derived Inducible Nitric Oxide Synthase Dimerization Inhibitors. *J. Med. Chem.* 2007; 50:1146-1157.

(30) Suaifan G., Goodyer C. L. M. and Threadgill M. D. Synthesis of N-(Methoxycarbonylthienylmethyl)thioureas and Evaluation of Their Interaction with Inducible and Neuronal Nitric Oxide Synthase. *Molecules* 2010;

15:3121-3134.

(31) Li H., Flinspach M. L., Igarashi J., Jamal J., Yang W., Gómez-Vidal J. A., Litzinger E. A., Huang H., Erdal E. P., Silverman R. B. and Poulos, T. L. Exploring the binding conformations of bulkier dipeptide amide inhibitors in constitutive nitric oxide synthases. *Biochemistry* 2005; 44:15222-15229.

(32) Li H., Igarashi J., Jamal J., Yang W. and Poulos T. L. Structural studies of constitutive nitric oxide synthases with diatomic ligands bound. *J. Biol. Inorg. Chem.* 2006; 11:753-768.

(33) Flinspach M., Li H., Jamal J., Yang W., Huang H., Silverman R. B. and Poulos, T. L. Structures of the neuronal and endothelial nitric oxide synthase heme domain with D-nitroarginine-containing dipeptide inhibitors bound. *Biochemistry* 2004; 43:5181-5187.

(34) Igarashi J., Li H., Jamal J., Ji H., Fang J., Lawton G. R., Silverman R. B. and Poulos, T. L. Crystal structures of constitutive nitric oxide synthases in complex with de novo designed inhibitors. *J. Med. Chem.* 2009; 52:2060-2066.

(35) Beeley N. R. A. and Sage C. GPCRs: an update on structural approaches to drug discovery. *Targets* 2003; 2:19-25.

(36) Steuber H., Zentgraf M., Gerlach C., Sotriffer C. A., Heine A. and Klebe, G. Expect the unexpected or caveat for drug designers: Multiple structure determinations using aldose reductase crystals treated under varying soaking and co-crystallisation conditions. *J. Mol. Biol* 2006; 36:174-187.

(37) Stubbs M. T., Reyda S., Dullweber F., Moller M., Klebe G., Dorsch D., Mederski W. and Wurziger H. pH-dependent binding modes observed in trypsin crystals: Lessons for structure-based drug design. *Chem. biochem.* 2002; 3:246-249.

(38) Klebe G. Virtual ligand screening: strategies, perspectives and limitations. *Drug Discov.Today.* 2006: 11:580-594.

(39) DePristo M. A., de Bakker P. I. W. and Blundell T. L. Heterogeneity and Inaccuracy in Protein Structures Solved by X-Ray Crystallography. *Structure* 2004; 12:831-838.

(40) Taha M. O., Bustanji Y., Al-Ghussein M. A. S., Mohammad M., Zalloum H., Al-Masri I. M. and Atallah, N. Pharmacophore Modeling, Quantitative Structure–Activity Relationship Analysis, and in Silico Screening Reveal Potent Glycogen Synthase Kinase-3β Inhibitory Activities for Cimetidine, Hydroxychloroquine, and Gemifloxacin. *J. Med. Chem.* 2008; 51:2062-2077.

(41) Al-masri I. M., Mohammad K. M. and Taha M. O. Discovery of DPP IV Inhibitors by Pharmacophore Modeling and QSAR Analysis followed by in silico Screening. *Chem.med.chem.* 2008; 3:1763-1779.

(42) Taha M. O., Dahabiyeh L. A., Bustanji Y., Zalloum H. and Saleh, S. Combining Ligand-Based Pharmacophore Modeling, Quantitative Structure−Activity Relationship Analysis and in Silico Screening for the Discovery of New Potent Hormone Sensitive Lipase Inhibitors. *J. Med. Chem.* 2008; 51:6478-6494.

(43) Taha M. O., Atallah N. and Al-Bakri A. G. Paradis-Bleau, C., Zalloum, H., Younis, K. S., Levesque, R. C., Discovery of new MurF inhibitors via pharmacophore modeling and QSAR analysis followed by in-silico screening. *Bioorgan. Med. Chem.* 2008; 16:1218-1235.

(44) Taha M. O., Bustanji Y., Al-Bakri A. G., Yousef A.-M., Zalloum W. A., Al-Masri I. M. and Atallah, N. Discovery of new potent human protein tyrosine phosphatase inhibitors via pharmacophore and QSAR analysis followed by in silico screening. *J. Mol. Graph. Model.* 2007; 25:870-884.

(45) Abu Hammad A. M. and Taha M. O. Pharmacophore Modeling, Quantitative Structure−Activity Relationship Analysis, and Shape-Complemented in Silico Screening Allow Access to Novel Influenza Neuraminidase Inhibitors. *J. Chem Inf. Model.* 2009; 49:978-996.

(46) Abu Khalaf R., Abu Sheikha G., Bustanji Y. and Taha M. O. Discovery of new cholesteryl ester transfer protein inhibitors via ligand-based pharmacophore modeling and QSAR analysis followed by synthetic exploration. *European J. Med. Chem.* 2010; 45:1598-1617.

(47) Al-Nadaf A. H. and Taha M. O. Discovery of new renin inhibitory leads via sequential pharmacophore

modeling, QSAR analysis, in silico screening and in vitro evaluation. *J. Mol. Graph. Model.*2011; 29:843-864.

(48) Al-Najjar B. O., Wahab H. A., Tengku Muhammad T. S., Shu-Chien A. C., Ahmad Noruddin N. A. and Taha M. O. Discovery of new nanomolar peroxisome proliferator-activated receptor (gamma) activators via elaborate ligand-based modeling. *European J. Med. Chem.* 2011; 46:2513-2529.

(49) Abdula A. M., Khalaf R. A., Mubarak, M. S. and Taha M. O. Discovery of new β-D-galactosidase inhibitors via pharmacophore modeling and QSAR analysis followed by in silico screening. *J. Comput. Chem.* 2011; 32:463-482.

(50) Abu Khalaf R., Abdula A. M., Mubarak M. S. and Taha M. O. Discovery of new β-D-glucosidase inhibitors via pharmacophore modeling and QSAR analysis followed by in silico screening. *J. Mol. Model.* 2011; 17:443-464.

(51) Discovery Studio Version 2.5 (DS 2.5) User Manual. Accelrys Inc, San Diego, CA, 2009. In 2009.

(52) Taha M. O., Tarairah M., Zalloum H. and Abu-Sheikha G. Pharmacophore and QSAR modeling of estrogen receptor (beta) ligands and subsequent validation and in silico search for new hits. *J. Mol. Graph. Model.*2010; 28:383-400.

(53) Ji H. T., Li H. Y., Martasek P., Roman L. J., Poulos T. L. and Silverman R. B. Discovery of Highly Potent and Selective Inhibitors of Neuronal Nitric Oxide Synthase by Fragment Hopping. *J. Med. Chem.* 2009; 52:779-797.

(54) Ji H., Stanton B. Z., Igarashi J., Li H., Martásek P., Roman L. J., Poulos T. L. and Silverman, R. B. Minimal Pharmacophoric Elements and Fragment Hopping, an Approach Directed at Molecular Diversity and Isozyme Selectivity. Design of Selective Neuronal Nitric Oxide Synthase Inhibitors. *J. Am. Chem. Soc.* 2008; 130:3900-3914.

(55) Lawton G. R., Ranaivo H. R., Chico L. K., Ji H. T., Xue F. T., Martase P., Roman L. J., Watterson D. M. and Silverman, R. B. Analogues of 2-aminopyridine-based selective inhibitors of neuronal nitric oxide synthase with increased bioavailability. *Bioorgan. Med. Chem.*

2009; 17:2371-2380.

(56) Hah J.-M., Martásek P., Roman L. J. and Silverman R. B. Aromatic Reduced Amide Bond Peptidomimetics as Selective Inhibitors of Neuronal Nitric Oxide Synthase. *J. Med. Chem.* 2003; 46:1661-1669.

(57) Ji H. T., Li H. Y., Flinspach M., Poulos T. L. and Silverman, R. B. Computer modeling of selective regions in the active site of nitric oxide synthases: Implication for the design of isoform-selective inhibitors. *J. Med. Chem.* 2003; 46:5700-5711.

(58) Mbadugha B. N. A., Seo J., Ji H. T., Martasek P., Roman L. J., Shea T. M., Li H. Y., Poulos T. L. and Silverman, R. B. Hydroxyl-terminated peptidomimetic inhibitors of neuronal nitric oxide synthase. *Bioorgan. Med. Chem.* 2006; 14:3681-3690.

(59) Seo J., Igarashi J., Li H., Martásek P., Roman L. J., Poulos T. L. and Silverman, R. B. Structure-Based Design and Synthesis of Nω-Nitro-l-Arginine-Containing Peptidomimetics as Selective Inhibitors of Neuronal Nitric Oxide Synthase. Displacement of the Heme Structural Water. *J. Med. Chem.* 2007; 50:2089-2099.

(60) Zhang H. Q., Fast W., Marletta M. A., Martasek P. and Silverman, R. B. Potent and selective inhibition of neuronal nitric oxide synthase by N-omega-propyl-L-arginine. *J. Med. Chem.* 1997; 40:3869-3870.

(61) Lee Y., Martasek P., Roman L. J., Masters B. S. S. and Silverman, R. B. Imidazole-containing amino acids as selective inhibitors of nitric oxide synthases. *Bioorgan. Med. Chem.* 1999; 7: 1941-1951.

(62) Lee Y., Martasek P., Roman L. J. and Silverman R. B. 1H-pyrazole-1-carboxamidines: New inhibitors of nitric oxide synthase. *Bioorgan. Med. Chem. Letters* 2000; 10:2771-2774.

(63) Huang H., Martasek P., Roman L. J. and Silverman R. B. Synthesis and evaluation of peptidomimetics as selective inhibitors and active site probes of nitric oxide synthases. *J. Med. Chem.* 2000; 43:2938-2945.

(64) Silverman R. B., Huang H., Marletta M. A. and Martasek, P. Selective inhibition of neuronal nitric oxide synthase by N-omega-nitroarginine- and phenylalanine-containing dipeptides and dipeptide

esters. *J. Med. Chem.* 1997; 40:2813-2817.

(65) Huang H., Martasek P., Roman L. J., Masters, B. S. S. and Silverman, R. B. Nω-Nitroarginine-Containing Dipeptide Amides. Potent and Highly Selective Inhibitors of Neuronal Nitric Oxide Synthase. *J. Med. Chem.* 1999; 42:3147-3153.

(66) Al-Nadaf A., Sheikha G. A. and Taha M. O. Elaborate ligand-based pharmacophore exploration and QSAR analysis guide the synthesis of novel pyridinium-based potent (beta)-secretase inhibitory leads. Bioorgan. Med. Chem. 2010; 18:3088-3115.

(67) Ramsey F. L. and Schafer D. W. The Statistical Sleuth: a Course in Methods of Data Analysis, first ed. Wadsworth Publishing Company, Belmont, CA, 1997 .

(68) Fischer R. The Principle of Experimentation Illustrated by a Psycho-Physical ExpeHafner Publishing Co, eighth ed. *Hafner Publishing*, New York, 1966.

(69) Verdonk M. L, Berdini V., Hartshorn M. J., Mooij W. T. M., Murray C. W., Taylor R. D. and Watson, P. Virtual screening using proteineligand docking: avoiding artificial enrichment, J *Chem. Inf. Comp. Sci.* 2004; 44: 793-806.

(70) Kirchmair J., Markt P., Distinto S., Wolber G. and Langer T. Evaluation of the performance of 3D virtual screening protocols: RMSD comparisons, enrichment assessments, and decoy selection e what can we learn from earlier mistakes? *J. Comput. Aided. Mol. Des.* 2008; 22: 213-228.

(71) Lipinski C. A., Lombardo F., Dominy B. W. and Feeney P. J. Experimental and computational approaches to estimate solubility and permeability in drug discovery and development settings. *Adv. Drug. Deliver. Rev.* 2001; 46: 3-26.

(72) Veber D. F., Johnson S. R., Cheng H. Y., Smith B. R., Ward K. W. and Kopple K. D. Molecular Properties That Influence the Oral Bioavailability of Drug Candidates. *J. Med. Chem.* 2002; 45:2615-2623.

QSAR

الدراسات　　　　　(eNOS)

.

151

(eNOS)　　　　10

(pharmacophore)

genetic algorithm
pharmacophoric models

(QSAR)　　　　　　　:

$(r^2_{121} = \mathbf{0.77}, F = \mathbf{63.5}, r^2_{LOO} = \mathbf{0.62}, r^2_{PRESS} = \mathbf{0.63})$

(pharmacophore)

(ROC)

.

(QSAR)　　　　　　　　(NCI)

.

:
.